Fast and slow rotators in the densest environments: a SWIFT IFS study of the Coma cluster

R. C. W. Houghton,[1]* Roger L. Davies,[1] F. D'Eugenio,[1] N. Scott,[2] N. Thatte,[1] F. Clarke,[1] M. Tecza,[1] G. S. Salter,[3] L. M. R. Fogarty[4] and T. Goodsall[1]

[1]*Physics Department, University of Oxford, Denys Wilkinson Building, Keble Road, Oxford OX1 3RH, UK*

[2]*Centre for Astrophysics and Supercomputing, Swinburne University of Technology, PO Box 218, Hawthorn VIC 3122, Australia*

[3]*School of Physics, The University of New South Wales, Sydney, NSW 2052, Australia*

[4]*Sydney Institute for Astronomy (SIfA), School of Physics, The University of Sydney, NSW 2006, Australia*

ABSTRACT

We present integral field spectroscopy of 27 galaxies in the Coma cluster observed with the Oxford Short Wavelength Integral Field specTrograph (SWIFT), exploring the kinematic morphology–density relationship in a cluster environment richer and denser than any in the ATLAS[3D] survey. Our new data enables comparison of the kinematic morphology relation in three very different clusters (Virgo, Coma and Abell 1689) as well as to the field/group environment. The Coma sample was selected to match the parent luminosity and ellipticity distributions of the early-type population within a radius 15 arcmin (0.43 Mpc) of the cluster centre, and is limited to $r' = 16$ mag (equivalent to $M_K = -21.5$ mag), sampling one third of that population. From analysis of the $\lambda - \epsilon$ diagram, we find 15 ± 6 per cent of early-type galaxies are slow rotators; this is identical to the fraction found in the field and the average fraction in the Virgo cluster, based on the ATLAS[3D] data. It is also identical to the average fraction found recently in Abell 1689 by D'Eugenio et al. Thus, it appears that the *average* slow rotator fraction of early-type galaxies remains remarkably constant across many different environments, spanning five orders of magnitude in galaxy number density. However, within each cluster the slow rotators are generally found in regions of higher projected density, possibly as a result of mass segregation by dynamical friction. These results provide firm constraints on the mechanisms that produce early-type galaxies: they must maintain a fixed ratio between the number of fast rotators and slow rotators while also allowing the total early-type fraction to increase in clusters relative to the field. A complete survey of Coma, sampling hundreds rather than tens of galaxies, could probe a more representative volume and provide significantly stronger constraints, particularly on how the slow rotator fraction varies at larger radii.

Key words: galaxies: clusters: individual: Coma – galaxies: elliptical and lenticular, cD – galaxies: evolution – galaxies: formation – galaxies: kinematics and dynamics.

1 INTRODUCTION

Studying the mechanisms that give rise to different galaxy morphologies is central to understanding galaxy formation and evolution. Although considerable progress has been made in reproducing the global characteristics of both late-type galaxies (LTGs) and early-type galaxies (ETGs), the picture is far from complete.

A source of confusion for such studies is the fact that visual morphologies do not always map simply to physical characteristics, particularly for the ETGs. The lenticular and elliptical division is not only difficult to measure quantitatively (for it is most commonly

made by eye, which is difficult to link to models), but is now known to be degenerate with regard to certain intrinsic properties of the galaxies: for example, the SAURON and ATLAS[3D] surveys (Bacon et al. 2001; Cappellari et al. 2011a) found the velocity maps of many ellipticals to be indistinguishable from those of S0s. Furthermore, the same authors identified a clear division in the properties of the velocity maps: most exhibited rapid disc-like rotation, while others showed little or no rotation, leading to the classifications *fast rotator* (FR) and *slow rotator* (SR). These classifications (and sub-classes, see Krajnović et al. 2008, 2011) are based on quantitative analysis of the morphology of velocity maps.

Combining λ (a proxy for the specific angular momentum) with ellipticity (ϵ), the $\lambda - \epsilon$ diagram takes on a similar role to the $V/\sigma - \epsilon$ diagram (Binney 1978; Davies et al. 1983; Binney 2005) and can be

* E-mail: rcwh@astro.ox.ac.uk

used to relate the FRs to a family of oblate axisymmetric spheroids (Cappellari et al. 2007; Emsellem et al. 2011). The anisotropy of these oblate spheroids is consistent with flattening along the axis perpendicular to the plane of rotation (z): flatter galaxies are more anisotropic. Projection effects can then explain the region of the $\lambda-\epsilon$ diagram occupied by the FRs (by assuming a Gaussian distribution of intrinsic ellipticities together with an upper limit in the anisotropy). However, the SRs are not represented by such models. They are an entirely different class of object and may be mildly triaxial (Emsellem et al. 2011).

The prevalence of ETGs in denser, crowded environments (such as galaxy clusters) has long been known (Oemler 1974; Davis & Geller 1976) with Dressler (1980) parameterising observational evidence in the morphology–density ($T-\Sigma$) relation. However, environment is not adequately described by a single parameter, such as projected density. As discussed by Muldrew et al. (2012), there are many different environments, and many different measures of environment. It is also important to realize that there are environments within environments: a massive, dense galaxy cluster may contain under dense regions. This latter case is of particular interest given the results presented later and we find it useful to define the *global host environment* (GHE, such as field, group or cluster) and the *local point environment* (LPE, such as the projected density at the position of a particular galaxy). GHE indicates the scale of largest (host) dark matter halo in the system, while LPE reflects the environment at the precise location of the galaxy in question. Using these definitions, galaxies in the Coma cluster have a cluster GHE, but could have very different LPEs. Similarly, the $T-\Sigma$ relation tells us how the relative fractions of ellipticals, S0s and Spirals changes with LPE; we remain ignorant about changes with GHE unless we assume a link between LPE and GHE (clusters are more likely to harbour denser LPEs).

Cappellari et al. (2011b) revisited the $T-\Sigma$ problem in light of the new SR and FR classification scheme. The updated kinematic morphology–density relation ($kT-\Sigma$) has similar properties to the original: the number of spirals decreases as the number of ETGs increases at higher densities. However, the overall fractions of FRs and SRs do not behave in the same manner. While the overall fraction of FRs increases in response to the decrease in the overall fraction of spirals, the overall fraction of SRs increases much more slowly. In fact, when we consider just the fraction of SRs in the ETG population (which we hereafter refer to as the SR fraction or f_{SR}), it is independent of the LPE density except for a sudden increase at the highest densities from around 15 to 25 per cent (cf. Fig. 8, Cappellari et al. 2011b). The data at high densities are dominated by galaxies in the core of the Virgo cluster (the densest LPE probed in ATLAS[3D]). Unlike the original $T-\Sigma$ relation which was composed entirely of cluster galaxies from 55 rich clusters, the $kT-\Sigma$ relation of Cappellari et al. (2011b) includes only one spiral-rich unrelaxed cluster, Virgo. We are thus almost completely ignorant of the kinematic–morphology density relation in clusters like those used to derive the original $T-\Sigma$ relation.

In light of the f_{SR} increase at the highest densities probed by ATLAS[3D], and the small number of clusters in the $kT-\Sigma$ relation, it is important to study the $kT-\Sigma$ relation of other clusters to investigate why the SR fraction suddenly increases in the core of Virgo and whether the SR fraction is truly independent of LPE density or GHE density (the average density of the host environment). D'Eugenio et al. (2013) performed an integral field spectroscopy (IFS) survey of Abell 1689 at $z = 0.183$ to investigate the $kT-\Sigma$ relation for one of the most massive and densest clusters known. Using the multiplexed IFS capability of the European Southern Ob-

servatory (ESO) FLAMES/GIRAFFE instrument, they identified that the average SR fraction of Abell 1689 is the same as for Virgo (no change with GHE) and that the fraction of SRs is enhanced in the densest regions and depleted in the lowest density regions of both clusters (i.e. a trend with LPE). Dynamical friction was proposed as an explanation for the segregation and the sudden increase in the SR fraction in the ATLAS[3D] $kT-\Sigma$ diagram. However, the degree of segregation in Abell 1689 is stronger than in Virgo. Both clusters are extremes: Abell 1689 is one of the most massive clusters known, and Virgo an unrelaxed low-mass cluster. Furthermore, current statistics on SRs are poor because they are rare.

We present IFS of 27 galaxies in the Coma cluster ($z = 0.024$, Han & Mould 1992) observed with the Oxford Short Wavelength Integral Field specTrograph (SWIFT, Thatte et al. 2006) to study the SR fraction and the SR segregation in a more typical cluster. We take special care to sample the galaxies without significant bias in luminosity or ellipticity which are known to affect the SR fraction directly. Throughout this work, we adopt a *Wilkinson Microwave Anisotropy Probe* 7 Cosmology (Komatsu et al. 2011); specifically, we use $H_0 = 70.4\,\mathrm{km\,s^{-1}\,Mpc^{-1}}$, $\Omega_m = 0.273$ and $\Omega_\Lambda = 0.727$. All quoted uncertainties are the standard 68 per cent confidence interval (CI) unless otherwise stated. The structure of this paper is as follows: Section 2 discusses the choice of the sample, the observations, the data reduction and the analysis techniques; Section 3 discussed uncertainties in derived quantities; Section 4 presents the kinematic maps, the $\lambda-\epsilon$ diagram for the Coma cluster and an updated $kT-\Sigma$ relation for Virgo, Coma and Abell 1689; Section 5 discusses the context of the results and Section 6 concludes.

2 DATA AND ANALYSIS

2.1 Sample selection

A complete survey of ETGs in a cluster is very observationally demanding, leading us to attempt inference from samples. Preliminary investigation revealed that f_{SR} could be estimated with an uncertainty of less than 10 per cent from a sample of 30 galaxies: approximating the distribution of SRs as binomial, we wish to infer f_{SR} (the probability of 'success') in a sample of n galaxies (the number of 'trials'); if the true fraction is f_{SR}, then the intrinsic variance for the number of SRs (around a mean $n f_{SR}$) is simply $n f_{SR}(1 - f_{SR})$ and the standard deviation about f_{SR} is $\sqrt{f_{SR}(1 - f_{SR})/n}$. Assuming $f_{SR} = 20$ per cent in a population of 30 galaxies, this approximation yields an inherent scatter of 7 per cent; such uncertainty is sufficient to distinguish between the core of Virgo (with $f_{SR} \sim 30$ per cent) and the average population (with $f_{SR} \sim 15$ per cent) to 95 per cent confidence. A more rigorous application of sample statistics is presented later in Section 3.3.2, where we correctly model uncertainties (without replacement) using a hypergeometric distribution; the assumption of a binomial distribution here is conservative as it overestimates the scatter in a sample (by a factor $\sqrt{(N - n)/(N - 1)}$, where N is the total number of galaxies in the population).

Without multiplexing, a survey of 30 galaxies is still demanding and requires observations spread over multiple semesters. The early results (described in Scott et al. 2012) consisted of IFS observations of 14 spectroscopically confirmed red sequence (RS) members of the Coma cluster. However, the selection was not representative of the parent luminosity or ellipticity distributions; rather they were chosen to have uniform representation in the logarithm of the galaxy velocity dispersion for greater diversity (wider sampling of the mass range). While this approach is useful for studying scaling relations

Table 1. Details of individual Coma galaxies in the sample. Colours, magnitudes, ellipticities and effective radii were measured using SDSS MONTAGE images, except for M_K which was measured from the 2MASS MONTAGE image. The $g' - r'$ colour is measured inside a 3.2 arcsec diameter; other magnitudes are Kron measurements. The ID is taken from Godwin, Metcalfe & Peach (1983). The specific angular momentum λ was measured from the *SWIFT* kinematic maps as described in the text; the value in parentheses gives the fraction of R_e over which the calculation was performed. The uncertainty in λ is the formal (random) uncertainty (see Section 1). The rotator class, C is defined as 0 for FRs, 1 for galaxies with λ below $0.31\sqrt{\epsilon}$ and 2 for morphologically identified SRs; a value of 3 corresponds to galaxies that are both classes 1 and 2. The probability of any galaxy being an SR is given by $p(SR)$ and is described in Section 3.3.1. The typical S/N in the binned *SWIFT* spectra (per 1 Å pixel) for each galaxy is given in the last column.

ID (GMP)	Σ_3 (kpc^{-2})	$g'-r'$ (mag)	$M_{r'}$ (mag)	M_K (mag)	ϵ	R_e (arcsec)	λ	C	$p(SR)$	S/N
2390	84.3	0.92 ± 0.01	-21.46 ± 0.002	-24.46 ± 0.006	0.214 ± 0.002	14.3	$0.16 \pm 0.03\ (0.2)$	0	0.22	41
2457	113.1	0.87 ± 0.02	-19.49 ± 0.004	-22.34 ± 0.016	0.416 ± 0.026	3.1	$0.38 \pm 0.02\ (1.0)$	0	0.00	18
2551	139.0	0.92 ± 0.02	-20.11 ± 0.003	-22.92 ± 0.013	0.452 ± 0.004	7.7	$0.35 \pm 0.01\ (1.0)$	0	0.00	14
2654	180.2	0.93 ± 0.01	-19.64 ± 0.004	-22.53 ± 0.015	0.142 ± 0.011	2.0	$0.21 \pm 0.01\ (1.0)$	0	0.00	18
2805	420.5	0.90 ± 0.01	-19.44 ± 0.005	-22.33 ± 0.017	0.221 ± 0.011	2.7	$0.31 \pm 0.01\ (1.0)$	0	0.00	18
2815	298.2	0.85 ± 0.01	-19.90 ± 0.004	-22.72 ± 0.014	0.510 ± 0.005	3.5	$0.40 \pm 0.04\ (1.0)$	0	0.00	22
2839	244.1	0.90 ± 0.01	-20.06 ± 0.004	-23.09 ± 0.012	0.080 ± 0.025	2.1	$0.29 \pm 0.01\ (1.0)$	0	0.00	23
2912	34.9	0.91 ± 0.01	-19.95 ± 0.004	-22.93 ± 0.013	0.289 ± 0.011	3.4	$0.29 \pm 0.01\ (1.0)$	0	0.00	19
2921	939.1	0.91 ± 0.01	-23.15 ± 0.001	-26.27 ± 0.003	0.359 ± 0.002	38.0	$0.04 \pm 0.01\ (0.1)$	3	1.00	48
2940	447.8	0.88 ± 0.01	-19.82 ± 0.004	-22.70 ± 0.014	0.066 ± 0.014	2.7	$0.32 \pm 0.03\ (1.0)$	0	0.00	10
2956	80.6	0.99 ± 0.01	-20.00 ± 0.004	-22.96 ± 0.012	0.640 ± 0.004	3.9	$0.50 \pm 0.01\ (1.0)$	0	0.00	18
2975	943.0	0.86 ± 0.01	-21.41 ± 0.002	-24.32 ± 0.007	0.022 ± 0.003	7.4	$0.09 \pm 0.01\ (1.0)$	2	0.00	19
3073	87.0	0.91 ± 0.01	-20.63 ± 0.003	-23.65 ± 0.009	0.151 ± 0.007	4.7	$0.22 \pm 0.02\ (1.0)$	0	0.00	17
3084	34.8	0.92 ± 0.01	-19.61 ± 0.004	-22.48 ± 0.016	0.124 ± 0.009	2.8	$0.13 \pm 0.01\ (1.0)$	0	0.07	17
3178	83.2	0.92 ± 0.01	-19.87 ± 0.004	-22.74 ± 0.014	0.299 ± 0.010	2.9	$0.24 \pm 0.01\ (1.0)$	0	0.00	12
3254	759.9	0.86 ± 0.02	-19.20 ± 0.005	-22.20 ± 0.019	0.300 ± 0.017	2.8	$0.32 \pm 0.02\ (1.0)$	0	0.00	13
3329	756.5	0.95 ± 0.01	-22.93 ± 0.001	-25.93 ± 0.003	0.115 ± 0.002	50.4	$0.08 \pm 0.02\ (0.2)$	3	0.92	33
3352	574.4	1.05 ± 0.01	-20.67 ± 0.003	-23.72 ± 0.009	0.082 ± 0.011	5.0	$0.30 \pm 0.02\ (1.0)$	0	0.00	25
3367	356.4	1.01 ± 0.01	-20.76 ± 0.003	-23.69 ± 0.009	0.230 ± 0.006	5.9	$0.41 \pm 0.03\ (1.0)$	0	0.00	24
3423	116.0	0.99 ± 0.01	-20.32 ± 0.004	-23.35 ± 0.011	0.429 ± 0.020	2.5	$0.41 \pm 0.01\ (1.0)$	0	0.00	23
3433	147.7	0.90 ± 0.02	-19.35 ± 0.005	-22.27 ± 0.017	0.318 ± 0.020	2.3	$0.16 \pm 0.02\ (1.0)$	1	0.68	13
3522	257.9	0.94 ± 0.01	-19.54 ± 0.005	-22.34 ± 0.017	0.127 ± 0.023	1.7	$0.26 \pm 0.01\ (1.0)$	0	0.00	19
3639	185.2	0.94 ± 0.01	-20.80 ± 0.003	-23.82 ± 0.009	0.285 ± 0.012	3.1	$0.24 \pm 0.02\ (1.0)$	0	0.00	26
3792	74.5	0.99 ± 0.01	-21.44 ± 0.002	-24.54 ± 0.006	0.162 ± 0.003	7.5	$0.07 \pm 0.04\ (1.0)$	3	0.89	34
3851	105.8	0.92 ± 0.02	-19.00 ± 0.005	-21.73 ± 0.022	0.226 ± 0.011	2.3	$0.31 \pm 0.02\ (1.0)$	0	0.00	12
3914	69.0	0.93 ± 0.01	-19.50 ± 0.005	-22.33 ± 0.017	0.121 ± 0.043	1.3	$0.26 \pm 0.02\ (1.0)$	0	0.00	15
3972	66.2	0.91 ± 0.01	-19.61 ± 0.004	-22.39 ± 0.016	0.187 ± 0.026	2.2	$0.18 \pm 0.01\ (1.0)$	0	0.00	13

(e.g. the Fundamental Plane; Djorgovski & Davis 1987; Dressler et al. 1987), it was the limiting factor in our ability to determine f_{SR} in the Coma cluster: the sampling uncertainty far outweighed the random uncertainty in our measurements and the bias to higher luminosities was difficult to correct for. To determine f_{SR} more accurately, we required a more representative sample, and as the sampling uncertainty drops to reasonable levels once the number of galaxies reaches around 30, we required another 16 galaxies, but chosen to alleviate bias. This 'second sample', together with the sample of Scott et al. (2012), is main subject of this paper.

Starting with SDSS sources within a 15 arcmin radius of the cluster centre (20 000 objects), we cross-matched all NED[1] galaxies with redshifts within ± 7000 km s^{-1} of $z = 0.024$ to create a spectroscopically confirmed sample of Coma cluster galaxies (377 objects). We then isolated the RS (see Section 2.5.1) in both this sample and the complete SDSS sample (over the same area of sky). Comparing the luminosity distributions of the RSs in both samples suggested that the spectroscopic data in NED was 50 per cent complete at $r' = 17.0$ mag. After forcing the selection of the Scott et al. sample, we selected a sample from the spectroscopic catalogue to match both the luminosity function and the ellipticity distribution of the parent sample (individual galaxies were chosen randomly,

subject to a few practical constraints such as ETG morphology and non-interaction with neighbours).

2.2 Photometric observations

We made use of the NASA/IPAC MONTAGE service[2] to mosaic SDSS images into a $1° \times 1°$ image, centred on the NED coordinates for the Coma cluster. The 2MASS images, resampled to the SDSS plate scale of 0.4 arcsec, required a zero-point correction of $5\log(0.4)$ mag to account for the change in scale. No further data reduction or cosmic ray removal steps were necessary.

2.3 Spectroscopic observations

The SWIFT instrument, mounted on the 200 inches (5 m) Hale telescope at the Palomar Observatory, was used to observe a total of 27 Coma galaxies (time constraints prevented us from observing 30 galaxies). Observations were made on the four separate observing runs on 2009 May 3–4, 2010 March 25–26, 2010 June 5 and 2012 May 9–14. Table 1 tabulates properties for the individual galaxies in the sample. Fig. 1 illustrates the SDSS r' apparent magnitudes of the parent and sample populations; there is little or no bias evident. A Kolmogorov–Smirnov test reports the probability of both
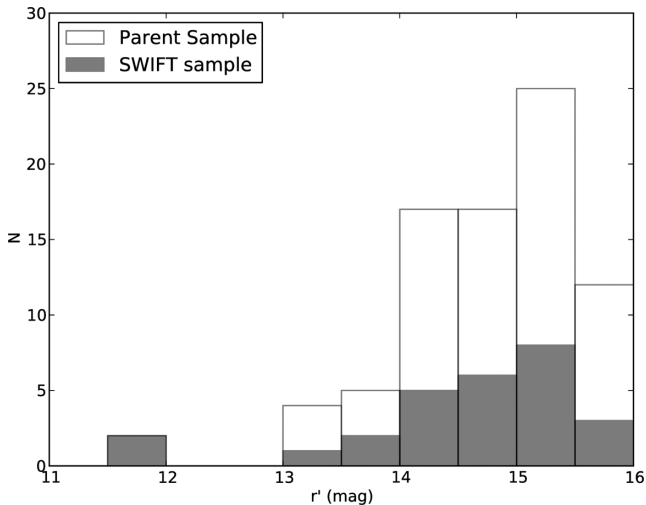
[1] NASA Extragalactic Database.

[2] http://montage.ipac.caltech.edu

Figure 1. The SDSS r' apparent magnitudes of the parent and sample populations; there is little or no bias evident in the luminosity function of the sample compared to the parent population. Given that we know that more luminous galaxies are more likely to be SRs, it is important for our sample to match the luminosity function of the cluster to avoid introducing bias into the derived f_{SR}.
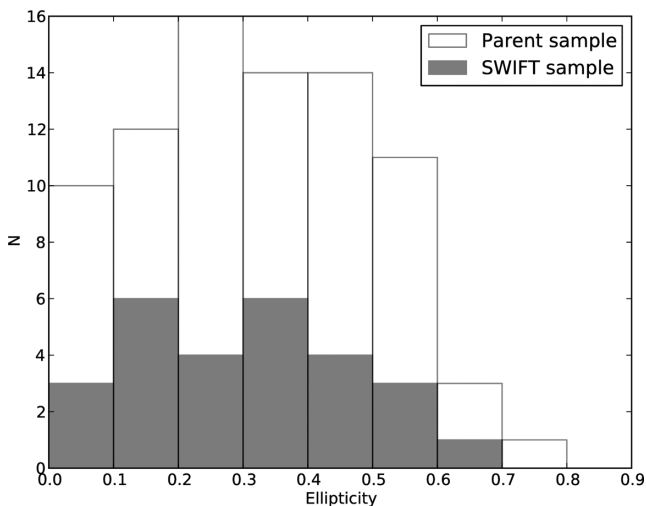

Figure 2. The SDSS r' de Vaucouleurs model ellipticites for the parent and sample populations; there is little or no bias evident in the ellipticity distributions of the sample compared to the parent population. Given that we know of no SRs with $\epsilon > 0.4$, it is crucial that our sample match the parent distribution of ellipticity to avoid introducing bias into f_{SR}.

samples being drawn from the same distribution to be 0.757. Similarly, Fig. 2 illustrates the SDSS r' de Vaucouleurs model ellipticites for the parent and sample galaxies; again, there is little or no bias present and a Kolmogorov–Smirnov test reports the probability of both samples being drawn from the same distribution to be 0.998.

2.4 Data reduction

The SWIFT data were reduced using the SWIFT data reduction pipeline, written for IRAF (Houghton, in preparation). The pipeline includes standard CCD data reduction steps such as bias subtraction, wavelength calibration and flat fielding as well as IFS specific stages such as cube reconstruction and illumination correction. The

final wavelength calibration is accurate to better than 0.1 Å. Cosmic rays are removed using the LACOSMIC routine (van Dokkum 2001). We correct for flexure along the spectral axis using the night sky emission lines. Sky emission was removed to first order (see Section 2.5.2) by subtracting sky frames adjacent in time to each science exposure; targets were either observed using the standard near-infrared 'ABBA' technique or using dedicated sky frames when the target occupied the full instrument field of view. Data cubes were combined using a dedicated PYTHON code, using offsets derived from the galaxy centroid in the wavelength-collapsed cubes. Although telluric standards were observed along with the science observations, no significant telluric absorption is present at the wavelengths used to calculate the kinematics so we do not attempt to correct for it.

2.5 Data analysis

2.5.1 Photometry

Integrated photometry was measured directly from the SDSS and 2MASS MONTAGE images in g', r' and K using SEXTRACTOR (v2.5.0). When calculating $g'-r'$, we used apertures of diameter 3.2 arcsec. Kron magnitudes were adopted as total magnitudes (for use in the colour–magnitude diagram and calculation of Σ_3). The same images were also used for variance/weight maps in SEXTRACTOR. Detailed masks were created to obscure bright stars and their diffraction spikes.

Using the SEXTRACTOR catalogues, we fit a double Gaussian mixture model to the RS and outlier distribution (using MCMC techniques as described in Houghton et al. 2012); this allows us to isolate RS galaxies in the cluster (the techniques used to clean the catalogues of stars and bad photometry are also described in Houghton et al. 2012). We chose an apparent magnitude limit of $r' < 16.2$ mag when fitting the colour–magnitude relation (CMR); a limit around 16 mag was desirable because this study aims to be comparable to ATLAS^{3D} (with $M_K < -21.5$ mag) but we found that SEXTRACTOR Kron magnitudes are slightly fainter (~ 0.2 mag) than the SDSS model magnitudes used in the selection process (Section 2.1); such systematic differences are to be expected (Graham et al. 2005). All objects within the 95 per cent CI of the derived CMR parameters were defined as *red* galaxies on the RS; 'outliers' above and below the RS were defined as 'extremely red' or 'blue', respectively. The resulting colour–magnitude diagram (CMD) is shown in Fig. 3. No spectroscopic information was used to correct for contamination by interlopers, although we do highlight spectroscopically confirmed cluster members (quoted by NED, see Section 2.1) in Fig. 3.

We derive the local surface density using all reliable detections (extremely red, red and blue) with $r' < 16.2$ mag. We define Σ_3 to be three times the reciprocal of the smallest circular area (A_3, measured in kpc^2 at the distance of Coma) that encloses the nucleus of the third nearest neighbour (with $M_K < -21.5$ mag). We must also make a correction for foreground /background galaxies which are not at the redshift of Coma. Using surveys of galaxy number counts (Yasuda et al. 2001), we estimate 2.4×10^{-3} galaxies per square arc min for $r' < 16$ mag. Thus,

$$\Sigma_3 = \frac{3 - (2.4 \times 10^{-3})a_3}{A_3}, \tag{1}$$

where a_3 is the same as A_3 but measured in square arc minutes. Note that we do not apply a constraint on the line-of-sight velocity as we have insufficient information for all photometric objects and furthermore, the velocity dispersion of the cluster is so high (~ 1000 km s^{-1}) that the usual constraint ($\Delta V_{los} < 300$ km s^{-1})
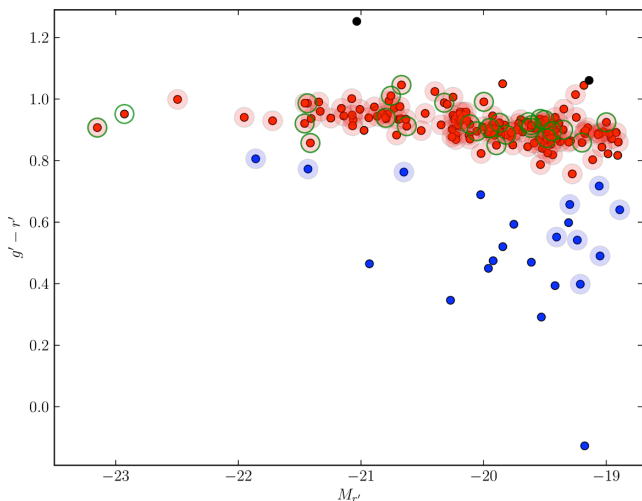
Figure 3. The CMD of the Coma cluster. Photometry was measured from the MONTAGE SDSS images using SEXTRACTOR. The RS was isolated using the techniques described in Houghton et al. (2012); red points refer to galaxies in the 95 per cent CI of the derived CMR, while black and blue points signify 'outliers' above and below the RS, respectively. Points with haloes are spectroscopically confirmed in NED. The green circles highlight the 27 SWIFT sample.

would be unsuitable. However, when considering the ETG population, as we do in Section 4, we take as a proxy all galaxies on the RS. We have not visually confirmed all red objects with $r' < 16.2$ mag to be ETGs. However, the SWIFT ETG sample was morphologically verified by eye, using the SDSS images. It is reassuring to see that all the SWIFT sample lies entirely on the RS in Fig. 3, adding confidence to the assumption that the RS traces ETGs. Clearly, this assumption may not be true in a field sample, but for a well evolved, low redshift cluster like Coma, there are very few exceptions, particularly in the central 15 arcmin as relevant to this study.

Surface photometry (ϵ, R_e and $\langle\mu_e\rangle$) was measured directly from the r' SDSS MONTAGE image. We integrated the pixel counts in circular apertures outwards from the centre and fitted the integral of the de Vaucouleurs profile to this curve of growth (described in Houghton et al. 2012) to determine the effective radius R_e and average effective surface brightness $\langle\mu_e\rangle$. The ellipticity ϵ was measured in a similar way to the SAURON and ATLAS^{3D} surveys: within the elliptical isophote of area πR_e^2, we calculated the second moments and the corresponding ellipticity.

2.5.2 Stellar kinematics and binning

We use the PPXF software (Cappellari & Emsellem 2004, v4.65) to calculate the stellar kinematics from the SWIFT spectra using the calcium triplet. We model the intrinsic line-of-sight velocity distribution of the galaxies with a Gaussian, parametrized by a first moment (velocity, V) and second moment (dispersion, σ). We provided PPXF with the Cenarro et al. (2001) library of stellar spectra (covering the range $0.8348 < \lambda(\mu m) < 0.902$). Accurate initial guesses for the systemic velocity were crucial to extract reliable kinematics; these were estimated by eye for each galaxy using the calcium triplet. We fit kinematics typically in the range $0.86 < \lambda(\mu m) < 0.89$ with small variations around $0.05\,\mu m$.

To optimize the extraction of kinematics across the galaxy, it was necessary to bin up spaxels to increase the signal to noise ratio (S/N). We chose a method based on azimuthal sectors (e.g. Nowak

et al. 2007; Rusli et al. 2011). After splitting the azimuthal angle into a pre-determined number of divisions, we adaptively binned spaxels, working outwards in radius, to achieve the desired S/N limit. In order to maximize spatial coverage, it was desirable to bin spectra up to the largest isophote which fitted inside the (co-added) field of view. However, in practice this was not always possible due to significant sky emission residuals progressively dominating over the source flux at larger radii. Therefore, the outer isophote level and corresponding radius were not fixed, but chosen individually for each galaxy: observations made under light cloud cover often exhibited larger sky residuals (both from strong and weak skylines), preventing us from binning out to larger and fainter isophotes. Similarly, the target S/N limit was not fixed: galaxies with a higher velocity dispersion required a higher S/N limit because the absorption features are shallower and more difficult to measure. Typical S/N limits ranged between 10 and 40 (per 1 Å pixel) and are listed in Table 1. Spaxels within a radius of 0.47 arcsec were binned to a single central aperture.

The spaxels from SWIFT do not have identical spectral resolutions. In order to match the resolution of the stellar library with the resolution of the galaxy observations, we measured the spectral resolution of the binned spectra using the skylines; we independently fit Gaussians to seven skylines surrounding the observed wavelength of the calcium triplet and chose the median full width at half-maximum as the formal resolution for that bin. In all binned spectra, the skylines were well represented by Gaussian profiles; no asymmetries, wings or top-hat profiles were apparent. We used this resolution as the instrumental resolution when deriving the kinematics of each bin with PPXF; typically σ_{inst} varied between 45 and 55 km s^{-1} across the field of view. Similarly, we also found deviations in the wavelength calibration of the order of a few km s^{-1}.

Exceptionally large sky line residuals can cause PPXF to find false solutions (particularly with respect to velocity). Although we made use of the CLEAN keyword in the PPXF software to reject highly deviant pixels (with just a single iteration), this was insufficient to ensure a robust solution. For this reason, we investigated masking the sky lines and simultaneously fitting the sky spectrum with the kinematics (as in Weijmans et al. 2009). This investigation is summarized in Appendix A3. We found that simultaneously fitting the sky emission gave the most robust kinematics with no obvious failures; masking sky lines did almost as well, but failed in a few cases.

While investigating the systematic uncertainty associated with the discretization of the kinematic maps (see Sections 3.1 and A2), we changed the binning geometry (by rotating the radial divisions of the sector patten and re-binning) and recalculated the kinematics. Averaging these multiple realizations provides a smoother representation of the data (hereafter referred to as the *dithered maps*), without formally smoothing the maps or the data cube (each binning realization has different radial divisions). Clearly the different kinematic realizations are correlated, but by perturbing the bin positions, we recover information on scales smaller than the size of the bins. This is best shown in the velocity map of GMP3423: in an individual realization, the wide azimuthal angle of the bins disperses (azimuthally) the velocity map extremities (the maximal rotation along the major axis); in the dithered map, the maximal rotation curve is confined to a narrower azimuthal width along the major axis. The use of dithering to recover information on scales smaller than the sampling is well documented [e.g. the DRIZZLE concept used to recover diffraction limited imaging from undersampled images on the *Hubble Space Telescope* (*HST*; Fruchter & Hook 2002)]. A

full exploration of this technique is beyond the scope of this work, and merits a separate investigation on its own. However, we find use for the dithered maps in calculating λ (see below).

2.5.3 Calculation of specific angular momentum, λ

We calculate λ following the approaches of the SAURON and ATLAS[3D] surveys. Briefly summarized, we use a circular de Vaucouleurs curve of growth method to measure R_e from the SDSS photometry (Section 2.5.1), find the elliptical isophote with area equal to πR_e^2 and calculate the moment ellipticity ϵ_e and position angle ϕ_e of the light falling within that isophote. Within an ellipse defined by these *effective* parameters ϵ_e and ϕ_e (again with area πR_e^2), centred on the first moment within the same aperture, we calculate λ as per the normal expression (Emsellem et al. 2011),

$$\lambda = \frac{\sum_i^N R_i F_i |V_i|}{\sum_i^N F_i R_i \left(V_i^2 + \sigma_i^2\right)^{1/2}}, \tag{2}$$

where R_i, F_i, V_i and σ_i are the radius, flux, velocity and velocity dispersion of the ith element and N is the number of elements enclosed within the $\{\epsilon_e, \phi_e, \pi R_e^2\}$ ellipse. We discuss the associated uncertainties in Section 3.

Where the ellipse defined by the effective parameters encompasses only a fraction of a bin, R_i and F_i are the mean radius and total flux of the enclosed portion of that bin. When the ellipse defined by the effective parameters was larger than the extent of the kinematic information, we calculate λ using the full map (we quote the fraction of R_e covered by our maps in Table 1). For such galaxies, we measure λ and ϵ on different scales. Comparison of data to the Virial Theorem (and its relatives) requires measurements to be made on the same scale (or mass fraction). Although this condition is not always met, for the few galaxies concerned ϵ does not vary strongly with radius and so would not change significantly if it were measured over the aperture defined by the kinematics maps.

We wish to classify ETGs as either fast or SRs. Most recently, this has been done with kinemetry (Krajnović et al. 2006, 2011). We investigate two approaches here. We can morphologically classify our data visually, like the SAURON survey, depending on whether the velocity map exhibits global, large-scale rotation or not. This is similar to the kinemetry approach, but lacks well-defined parametric limits. We can also use the division in the $\lambda-\epsilon$ plane: SRs appear to inhabit the region defined by $\lambda < 0.31\sqrt{\epsilon}$ (Emsellem et al. 2011). However, the uncertainties in λ and ϵ may not be negligible, as discussed below, so careful modelling of random and systematic uncertainties is required to robustly make use of this approach, particularly at higher redshifts (as was done in D'Eugenio et al. 2013).

3 ESTIMATES OF UNCERTAINTY

We propagate uncertainties by approximating the Poisson photon statistics with a normal distribution together with the first-order (derivative) approach. This neglects covariances introduced by interpolation of the data and provides uncertainties in integrated magnitudes, aperture colours and kinematics.[3]

---

[3] PPXF derives parameter uncertainties, based on the input uncertainties of the galaxy spectrum, using the Levenberg–Mardquart algorithm but it ignores the covariances with template mismatch and sky subtraction which are optimized outside of this algorithm.

3.1 Uncertainties in specific angular momentum, λ

In Appendix A, we investigate different contributions to the uncertainty in λ: the formal random uncertainty (from photon statistics) in deriving λ from a single realization (Section A1), the systematic uncertainty from discretization of the kinematic maps (Section A2), and the systematic uncertainty in the kinematics originating from sky line residuals (Section A3).

We find that the formal random uncertainty is typically the dominant source of uncertainty (we derive expressions for the first-order propagation of uncertainties in Section A1, which are not trivial). The discretization error is nearly always smaller than the formal random uncertainty and can be minimized further by using the dithered maps to calculate λ. However, the uncertainty from photon noise cannot be reduced by dithering so we adopt the *average* random uncertainty in λ calculated from single binning realizations (quoted in Table 1). Furthermore, when we fit the sky spectrum simultaneously with the kinematics, the systematic uncertainty from the sky residuals is greatly reduced (typically < 0.01 in λ) which is smaller than the formal random uncertainty.

3.2 Uncertainties in ϵ

When estimating ϵ, we quote the rms deviations from a polynomial fit to the ellipticity profile within the range $0.1 < R/R_e < 10$.

3.3 Uncertainties in f_{SR}

There are two principle sources of uncertainty when we infer f_{SR}. First, the accuracy of our observations leads to uncertainty in the number of SRs found in the sample; we call this measurement uncertainty. Secondly, there is uncertainty from using a finite sample; we call this sample uncertainty. We now discuss these uncertainties in the next two sections, followed by a discussion on how to combine them.

3.3.1 Measurement uncertainties

We have calculated uncertainties for both λ and ϵ; we now wish to propagate these uncertainties into our calculation of f_{SR}. When f_{SR} is estimated using morphological analysis of the kinematic maps, such propagation is unclear. However, if one classifies galaxies with $\lambda < 0.31\sqrt{\epsilon}$ as being SRs, the propagation of uncertainties can be approximated with Monte Carlo techniques, as in D'Eugenio et al. (2013).

Let us make the assumption that the true value of λ and ϵ for each galaxy is normally distributed around our measurements (with no correlation between λ and ϵ), using standard deviations defined by our uncertainty estimates. We must also truncate and renormalize the normal distributions to ensure that $0 < \lambda < 1$ and $0 < \epsilon < 1$. By sampling these distributions many times, we can infer the probability of any one galaxy having $\lambda < 0.31\sqrt{\epsilon}$ (quoted in Table 1 as $p(SR)$). Similarly, by sampling the distributions of all galaxies simultaneously, we can infer the probability of any number of the galaxies having $\lambda < 0.31\sqrt{\epsilon}$; this is important if many galaxies individually have quite low probabilities of being SRs, because the probability of any one of them being an SR may be significant.

3.3.2 Sample uncertainties

To put results from our sample into context, we should define the uncertainties associated with inferring quantities from a

(representative) subset of the population and similarly the uncertainties when inferring from the *complete* population. In the latter case, it is not true that complete samples are free from uncertainty: a finite sample drawn from a binomial distribution will always show variation in the number of 'successes' because the variance of that binomial distribution is non-zero. The type of uncertainty we choose to quote depends on the question we wish to answer; in the case of a subset of galaxies taken from Coma the obvious question is 'How many SRs are there likely to be in Coma (given a subset of galaxies with certain constraints on luminosity and environment)?' Thus here, we wish to 'correct' an analysis to infer the intrinsic value of some parameter *in the parent sample*. Conversely, we may ask the question 'Is the intrinsic f_{SR} of this population the same as other populations (given constraints on luminosity and environment)?' This is subtly different to the former question, but the solutions are similar as we now show.

Given a sample of n galaxies taken from population of N galaxies, let us attempt to infer the *true* number of SRs in the population K, given that we observed in our sample only k SRs. Formally, the hypergeometric distribution tells us the probability of finding k SRs in a sample of n from a parent population of N galaxies which actually has K SRs

$$p(k|n, K, N) = \frac{\binom{K}{k}\binom{N-K}{n-k}}{\binom{N}{n}}, \tag{3}$$

where $\binom{a}{b}$ is the binomial coefficient. To estimate the uncertainty on K, we must use Bayes theorem,

$$p(K|k, n, N) = \frac{p(K|n, N)p(k|n, K, N)}{p(k|K, N)}. \tag{4}$$

The term $p(K|n, N)$ is the prior. We use uninformative flat priors for K, allowing with equal probability $0 \leq K \leq N$. Furthermore, we calculate the denominator in equation (4) by requiring that $p(K|k, n, N)$ is normalized.

We can now estimate the uncertainty in the true number of SRs in the Coma cluster given our selection criteria, and with (or without) additional luminosity or environment constraints. In any given bin of luminosity or projected density, we only need to know the sample size n', the observed number of SRs in that bin k' and the actual number of galaxies from the cluster that fall into that bin N' to estimate the uncertainty in the true number of SRs K' using equation (4). However, in this way we estimate the uncertainty (actually the posterior) on the number of SRs only in *Coma*, given our selection criteria and any other assumptions we have made. We are *not* estimating the posterior for the number of SRs in the galaxy population as a whole, or even for clusters 'like Coma'. If we wished to do this, we should replace the hypergeometric distribution with the binomial, with a probability of 'success' $p = K/N$. Naturally, this is the large N limit when using the hypergeometric distribution for finite populations. Therefore, even for complete surveys such as ATLAS[3D], there is a posterior uncertainty associated with inferring f_{SR} for *all* ETGs in the Universe at $z \sim 0$, or for inferring f_{SR} in clusters *like* Virgo. We plot this uncertainty on the ATLAS[3D] data in Figs 7 and 8.

3.4 Combining measurement and sample uncertainties

We know that our measurements are uncertain and that inference from a sample (whether sparse or complete) also carries an uncertainty. If one were significantly larger than the other, we could neglect the smaller, but unfortunately that is not the case here. To reliably report on f_{SR} in the Coma cluster requires us to account for both these sources of uncertainty.

The technique described in Section 3.3.2 provides $p(K|k, n, N)$, which seems to provide an answer to how many SRs there are in the parent population. However, if our assumption about the value of k was incorrect, then this answer is also incorrect. The discussion in Section 3.3.1 highlights that our measurement of k is uncertain, and it describes how to estimate a *probability distribution* $p(k|n, N)$ for the number of SRs found in our sample. With this information, we can marginalize over all possible values of k to recover $p(K|n, N)$. Formally,

$$p(K|n, N) = \sum_i p(K|k_i, n, N)p(k_i|n, N), \tag{5}$$

where i indexes the possible values of k. If there were significant uncertainty in n and N, we could similarly integrate them out.

For Abell 1689, we can also combine the measurement uncertainty with the sample uncertainty, as $p(SR)$ is known for each galaxy. For the ATLAS[3D] data however, uncertainties on λ and ϵ were not published, so we can only quote $p(K|k, n, N)$ for these data in Figs 6 and 7; such uncertainties are likely to be underestimates.

4 RESULTS

Typical (binned) SWIFT spectra for each Coma galaxy are shown in Fig. 4. These examples illustrate the median quality (in terms of S/N) for each galaxy. They have not been corrected for individual recession velocities, allowing the quality of the sky subtraction (the dominant source of systematic error, see Section A) to be compared at each wavelength. We overplot the best-fitting kinematic model spectrum in red.

We present kinematic maps for the sample of 27 Coma cluster ETGs in Fig. 5. For each galaxy, the reconstructed image is shown with the dithered velocity and velocity dispersion maps. The colour bar scales for both the velocity and dispersion maps are fixed; this is to highlight the differences between the galaxies.

Fig. 6 shows the $\lambda-\epsilon$ diagram for our Coma sample. If we select SRs morphologically based on the absence of significant rotation, we find four examples: GMP2921, GMP3329, GMP3792 and GMP2975. If we classify SRs as all galaxies with $\lambda < 0.31\sqrt{\epsilon}$, then there are also four examples in Fig. 6: GMP2921, GMP3329, GMP3792 and GMP3433. Using the Monte Carlo techniques described in Section 3.3, we formally find $4\pm^{1.7}_{1.6}$ with $\lambda < 0.31\sqrt{\epsilon}$.

There are three galaxies that satisfy both the morphological and the $\lambda-\epsilon$ constraints (red in Fig. 6) and two galaxies that satisfy one or the other (yellow in Fig. 6). Table 1 summarizes these results. Thus, however we classify an SR, we find f_{SR} in the ETG population of Coma to be around 15 per cent. Emsellem et al. (2011) highlight that the $\lambda-\epsilon$ division is only representative and wherever possible, it is preferable to classify galaxies individually based on the appearance of the velocity map. Accordingly, hereafter we report on the number of morphological SRs ($C \geq 2$ in Table 1), but we derive corresponding uncertainties from the $\lambda-\epsilon$ diagram using the techniques described in Section 3.3.

GMP2921 and GMP3329 show no evidence of rotation and are undisputed SRs. Similarly GMP3792 and GMP2975 show no evidence of global rotation extending to large radii. All four of these morphological SRs have $\lambda < 0.1$. Although GMP2975 is consistent with being an FR in the $\lambda-\epsilon$ diagram ($\epsilon = 0.022$, $\lambda = 0.08$), suggesting that it is an oblate nearly isotropic ellipsoid seen face on, it does not show global rotation in its velocity map. Were it an FR, the necessary alignment along the line of sight would be extremely
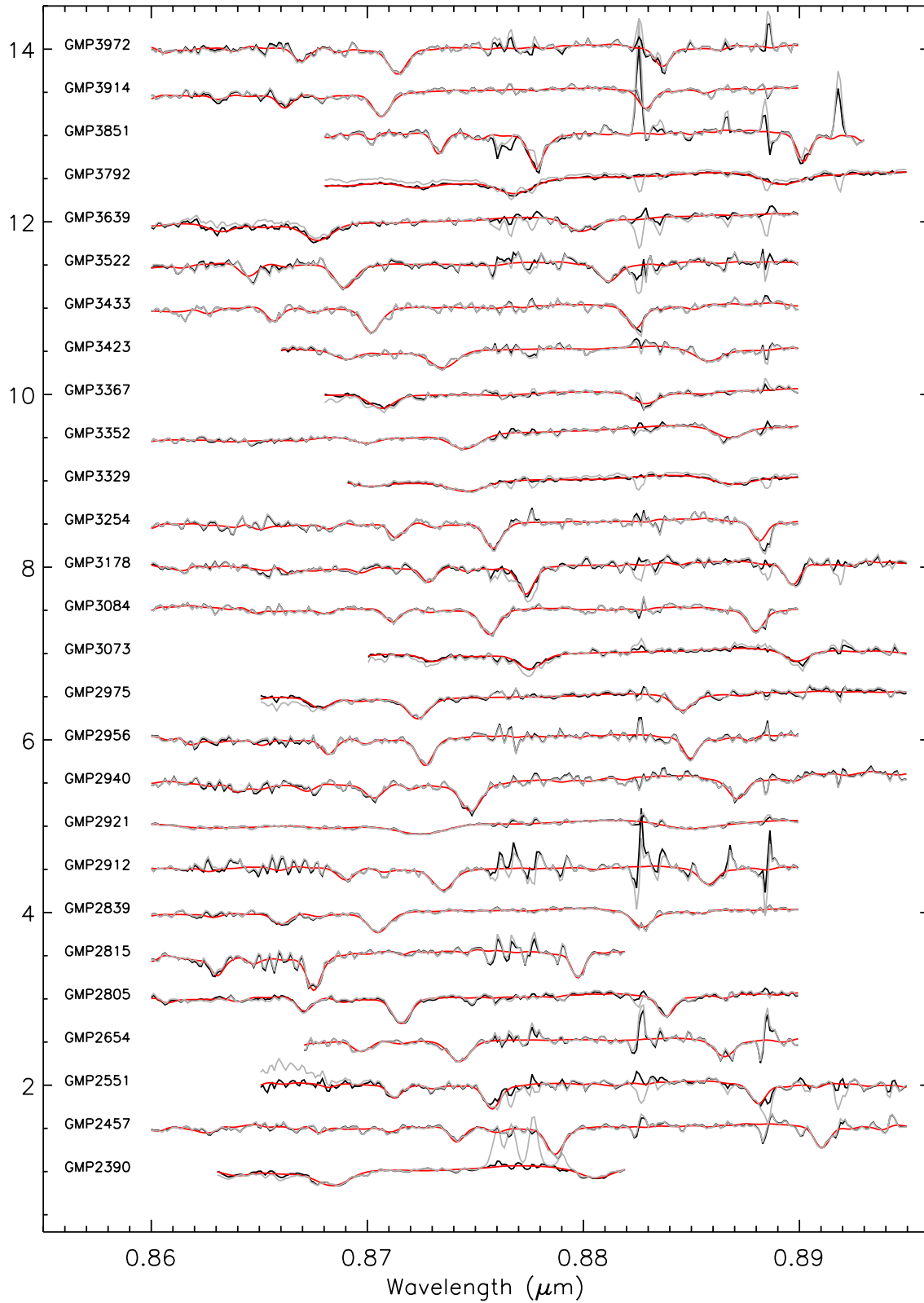
Figure 4. Typical spectra for the 27 galaxies in this sample. The spectra have not been corrected for recession velocity and are sorted by GMP number. Galaxy spectra in black are shown with optimized sky subtraction while galaxy spectra in grey show typical residuals using a first-order (standard) sky subtraction. The best-fitting kinematic model spectrum is shown in red for each spectrum. Spectra have been normalized by the (median) continuum level and are spaced vertically by intervals of 0.5.
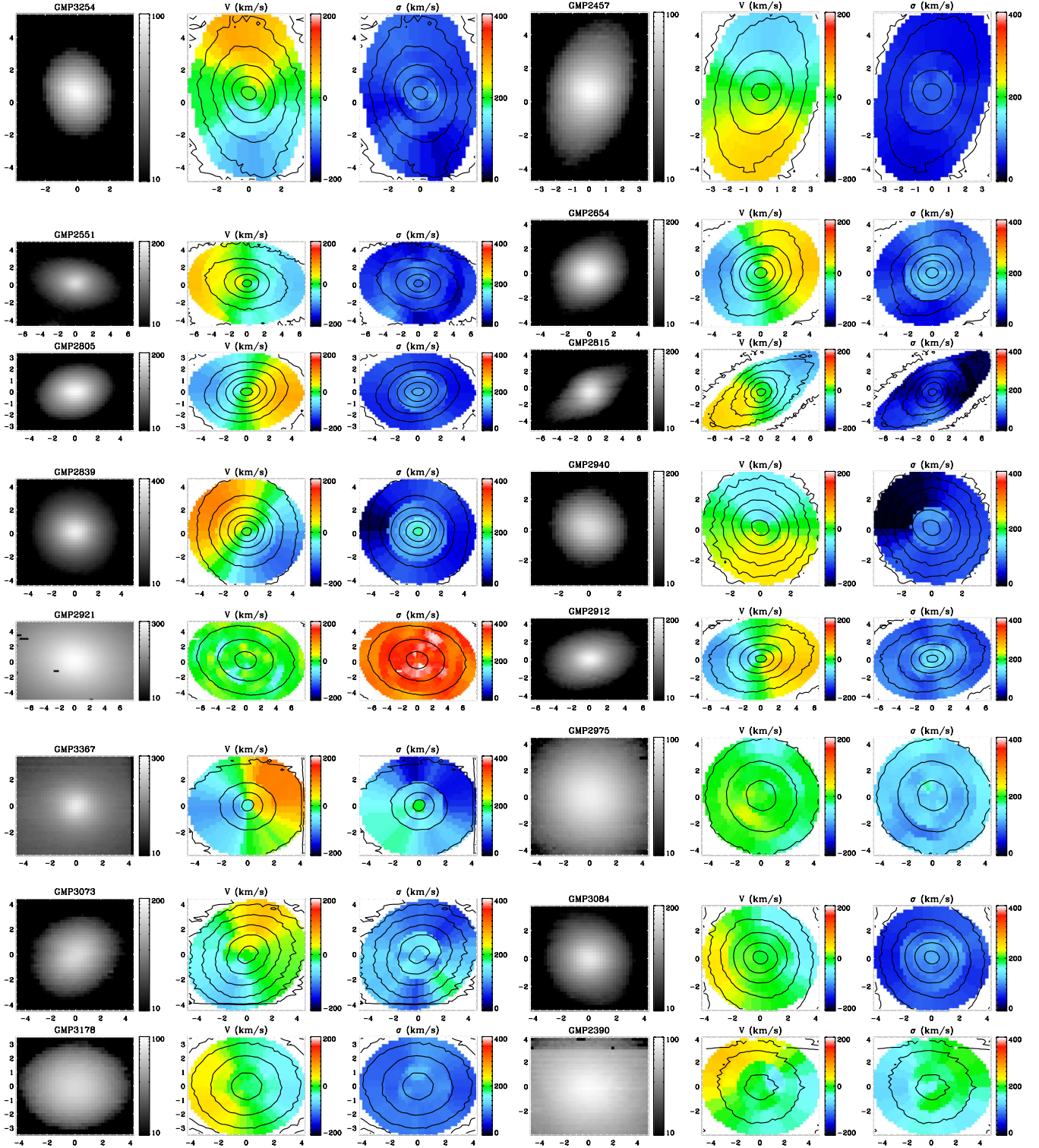
Figure 5. SWIFT kinematics for 27 ETGs in the Coma cluster. For each galaxy, three images are shown: the flux map, the dithered velocity map and the dithered velocity dispersion map. *X*-axis and *Y*-axis scales are given in arcseconds. The ordering of the galaxies is not strictly sorted by the GMP ID, but has been optimized to save space in the figure. The kinematic maps are averaged over many different binning realizations (see Section 2.5.2).

rare; in ATLAS[3D] (260 galaxies), no FR with $\{\lambda, \epsilon\} < 0.1$ was found (Emsellem et al. 2011). Assuming GMP2975 is an SR, either (underestimated) measurement error scattered it above $0.31\sqrt{\epsilon}$, or SRs are occasionally found above this fast/slow division.

The SRs we identify all have $\epsilon < 0.4$, consistent with the SRs in ATLAS[3D]. Conversely, all the FRs detected have $\lambda < 0.6$; a similar result was found in D'Eugenio et al. (2013). However, in ATLAS[3D] the FRs populate up to $\lambda < 0.8$.
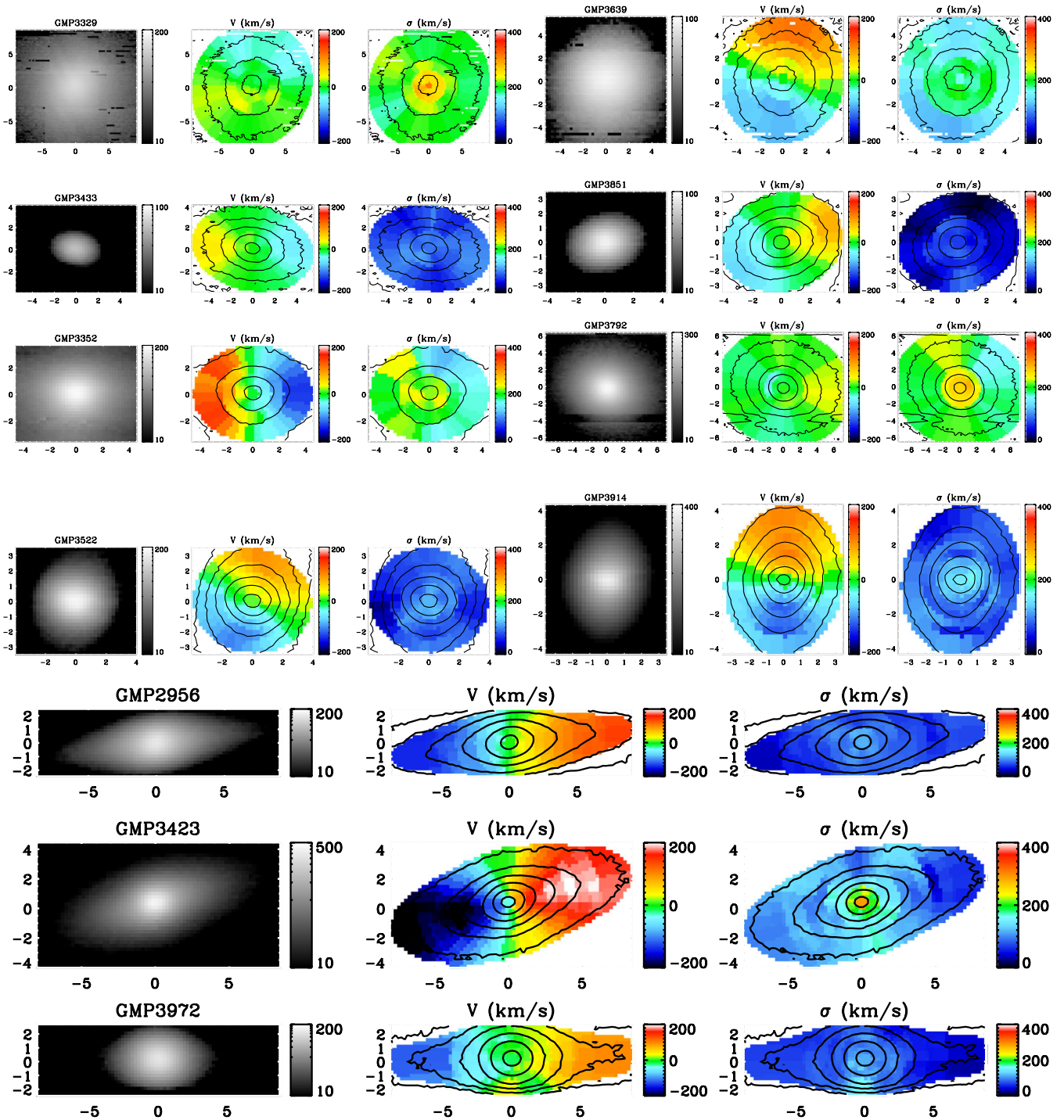
Figure 5 – *continued*

The majority of the dispersion maps in Fig. 5 are blue (dynamically cold, $\sigma < 100\,\mathrm{km\,s^{-1}}$), while one dispersion map stands out from all the others as being dynamically much hotter than the others; that of GMP2921. This galaxy is likely the most massive in the cluster and is one of the two central dominant galaxies. However, the other centrally dominant galaxy, GMP3329, has a very moderate dispersion map in comparison; indeed the dispersion map of the non-central galaxy GMP3792 is just as dynamically hot.

The dispersion maps do not universally show dynamically hotter components at their centres; indeed, they seem to show a range of radial gradients. GMP2457, GMP2551, GMP2975 and GMP3433 show no clear rise in dispersion towards their centres; conversely, GMP2839, GMP2912, GMP3423 and GMP3914 show clear evidence of a rise in dispersion. While the dispersion maps are in general noisier than the velocity maps, the strength of a central, dynamically hotter component can be judged in nearly all cases; the
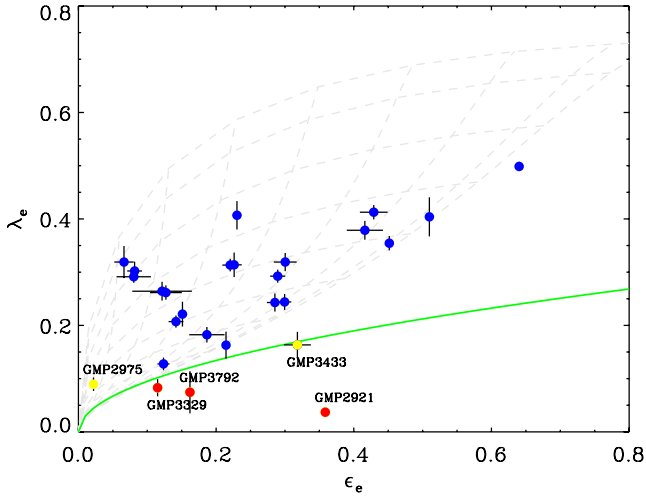
Figure 6. The $\lambda-\epsilon$ plot for the Coma cluster. The error bars represent random uncertainty only. The light grey grid projects oblate ellipsoid models (of increasing flattening and anisotropy) at various inclinations. The green line ($0.31\sqrt{\epsilon}$) represents a formal division between (projected) FRs and SRs in the ATLAS[3D] survey (Emsellem et al. 2011). We label all types of SRs; class 1 or 2 are coloured yellow while class 3 are coloured red. FRs are coloured blue.

Figure 7. The SR fraction (f_{SR}) in the ETG population as a function of absolute (2MASS) K magnitude: solid bars show the observed values while light shaded bars show the resulting uncertainty in the posterior. The entire ATLAS[3D] sample is shown in black; Virgo data from ATLAS[3D] is shown in blue; data for Abell 1689 is shown in green (D'Eugenio et al. 2013) and the Coma data (this survey) is shown in red. The (posterior) uncertainties shown for the ATLAS[3D] data assume a binomial distribution for f_{SR}, while the (posterior) uncertainties for Coma and Abell 1689 assume a hypergeometric distribution and account for measurement uncertainties (see Section 3).

exceptions are GMP2390, GMP3073, GMP3352 and GMP3357, where noise in the maps is sufficient to prevent clear identification of radial gradients.

We also find trends with the dispersion maps. Dynamically cold dispersion maps are associated with rotating velocity maps (FRs). Conversely, SRs are generally associated with dynamically hotter dispersion maps. However, dynamically hot dispersion maps are *not* always SRs. A concern for this rule is GMP2975, which we classify morphologically as an SR despite its position in the (FR region of the) $\lambda-\epsilon$ plot of Fig. 6; although having a relatively cool dispersion map, it is not technically 'cold' because $\sigma > 100\,\mathrm{km\,s^{-1}}$. Interestingly, there is no evidence of increasing dispersion towards the centre of this galaxy.

We present f_{SR} as a function of luminosity (M_K) density ($\log\Sigma_3$) in Figs 7 and 8, respectively. As discussed in Section 3, it is more useful to consider uncertainties on the posterior than on the likelihood, so we show the 68.2 per cent CI of the posterior probability. Posterior uncertainties are not the same as maximum-likelihood uncertainties. For example, the formal uncertainty on the posterior (we quote ±32.1 per cent from the median) may not encompass the actual observation. We could be informative here: we know f_{SR} in Abell 1689 is around 15 per cent (D'Eugenio et al. 2013); similarly, we know that SRs must have $\epsilon < 0.4$, providing an upper limit to f_{SR}. But we do not investigate these informative priors.

Fig. 7 confirms that SRs are more common than FRs at higher luminosities in all GHEs (field /group, Virgo, Coma or Abell 1689). We do not find any low-luminosity SRs in our sample (all SRs have $M_K < 24$ mag), although the finite probability of misclassifying these galaxies in the $\lambda-\epsilon$ plot (Fig. 6) leads the posterior to favour the presence of low-luminosity SRs at the 68 per cent confidence level. Specifically, the low-luminosity galaxy GMP3433 biases the posterior in this way; it is likely to originate from below $0.31\sqrt{\epsilon}$, although we classify it morphologically as an FR due to the clear rotation gradient in its velocity map. The posterior would not have been in favour of any low-luminosity SRs had we quoted the uncertainty from just a sample analysis $p(K|k, n, N)$.
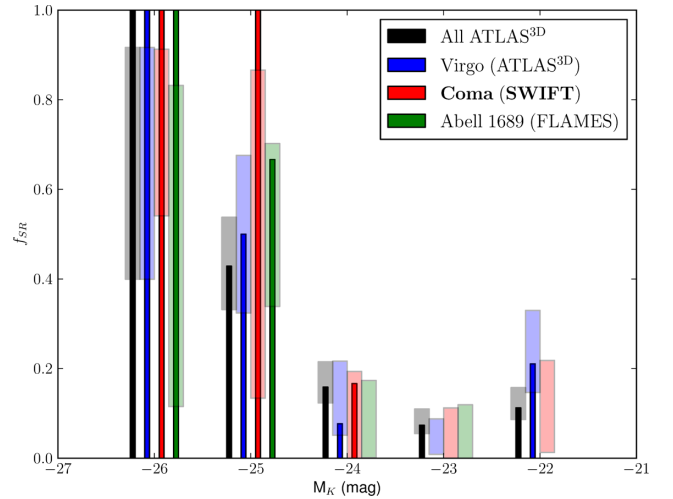
Fig. 8 shows that the *average* f_{SR} in different GHEs is remarkably constant at around 15 per cent. A simple linear fit with uncertainties in f_{SR} alone[4] provides a best fit of $f_{SR} = (0.009 \pm 0.02)\log\Sigma_3 + (0.14 \pm 0.02)$ and suggests that the slope is consistent with zero. Within individual clusters, there is strong evidence for an increase in f_{SR} in denser LPEs and similarly, a decrease in less dense LPEs; the evidence is particularly strong for Abell 1689 (D'Eugenio et al. 2013). Note however that the low-density LPE limit where only FRs are found is different for each cluster; while no SRs are found in Abell 1689 at an LPE density of $\log\Sigma_3 \sim 2.2$, the same LPE density in Virgo holds the highest f_{SR} in the entire cluster.

5 DISCUSSION

We presented a subset of our sample in (Scott et al. 2012). That subset did not sample the parent population fairly, but was biased to higher luminosities by design. Scott et al. (2012) found a higher f_{SR} than in this work, which is understood from the luminosity bias: SRs are more common than FRs for more luminous galaxies. In the full sample presented here, we took precautions to be unbiased with respect to luminosity and ellipticity.

If we consider the dependence on luminosity, Fig. 7 confirms previous findings that more luminous galaxies are more likely to be SRs. Furthermore, this trend is no stronger or weaker for cluster galaxies than it is for the field /group galaxies in the ATLAS[3D] survey, suggesting no dependence with GHE (except that the most luminous galaxies do not exist in the field /group environment of ATLAS[3D]). This suggests that the formation mechanism for SRs must be more efficient for more luminous galaxies, but equally so across different GHEs. Although we find no low-luminosity SRs,

---

[4] As described in section 15.2 of Press et al. (1992).
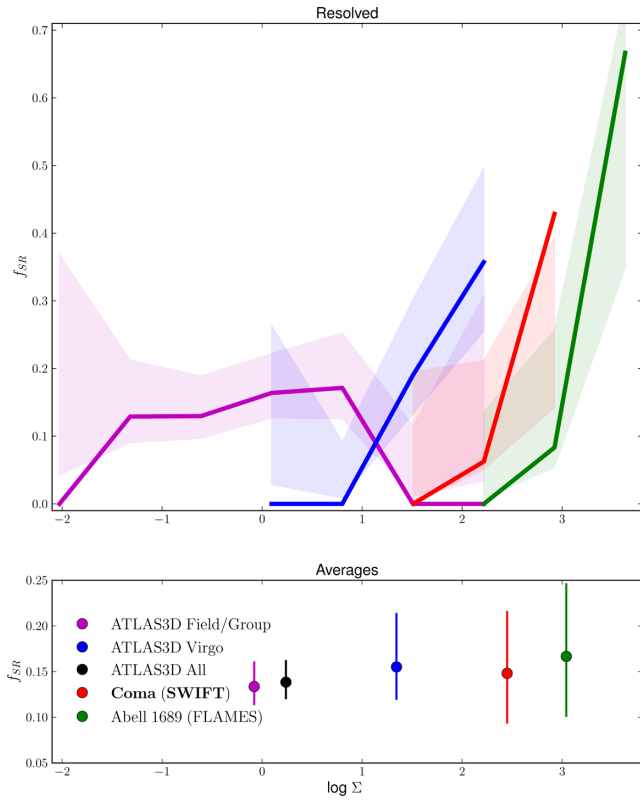
Figure 8. The SR fraction (f_{SR}) in the ETG population as a function of projected density ($\log\Sigma_3$). Upper: resolving f_{SR} as a function of projected LPE density for each GHE; solid lines refer to the observed quantities, while shaded regions refer to the posterior uncertainties. Lower: the average f_{SR} for the average projected density of each GHE; for Coma and Abell 1689, average GHE densities refer to the mean LPE of the samples, not the mean LPE of the parent distribution. All: the entire ATLAS[3D] volume-limited survey is shown in black; ATLAS[3D] data not in Virgo (field/group) is shown in magenta; ATLAS[3D] data for Virgo alone is shown in blue; the data for Abell 1689 is shown in green (D'Eugenio et al. 2013); the data for Coma from this survey is shown in red. The uncertainties shown for the ATLAS[3D] data assume a binomial distribution for f_{SR}, while the uncertainties for Coma and Abell 1689 assume a hypergeometric distribution and account for measurement uncertainties (see Section 3).

we sample enough low-luminosity galaxies to place reasonable constraints on f_{SR} down to $M_K = -21.5$ mag and there is a suggestion of a non-zero number of SRs at the lowest luminosities from the calculation of our posterior $p(K|n, N)$. This originates from measurement uncertainty; a low-luminosity FR (GMP3433) lies near the $\lambda-\epsilon$ division and the uncertainties in λ and ϵ are not insignificant.

Combining our results for Coma with those of Cappellari et al. (2011b) and D'Eugenio et al. (2013), we find the *average* f_{SR} in the ETG population is identical in the clusters studied so far (Virgo, Coma and Abell 1689). This is quite remarkable in itself, but even more remarkable is that this is the same as the average in the ATLAS[3D] field and group environment. There appears to be no variation in f_{SR} with GHE.

The morphology–density relation exists because ETGs are more prevalent in clusters, implying that the mechanism that produces ETGs is more efficient at higher (GHE) densities (Dressler 1980). We have shown that f_{SR} is uniform across *all* GHEs, which suggests that the mechanism that creates SRs shares exactly the same efficiency boost as the mechanism that produces FRs in a denser

GHE. If the two mechanisms are one and the same, this is a trivial consequence. But the structural differences between FRs and SRs strongly suggest different evolutionary histories and formation mechanisms. If one mechanism feeds off the success of the other (FRs might be transformed into SRs via merging), we might also expect to see a constant f_{SR}, so long as the mechanism efficiency (f_{SR}) is independent of the GHE density. Regardless, we now know that whatever formation mechanisms are proposed for FRs and SRs in the future, they must be independent of the GHE in which the ETGs are found today.

More insights can be gained from resolving clusters into subpopulations of different LPE density (Fig. 8). For Coma and Abell 1689, we see strong evidence that SRs are more likely to be present in the denser LPEs within a cluster. This is not a threshold effect: there is no special number density that catalyzes the formation of SRs. On the contrary, we see that galaxies in Abell 1689 with $\log\Sigma_3 \approx 2.2$ are unlikely to be SRs (below the cluster average), while galaxies at the same densities in Coma and Virgo have a higher chance of being SRs (above the cluster average). Given that these clusters share the same average f_{SR}, there must be a process that segregates SRs from the overall population, forcing them towards the densest regions of the cluster. As discussed in D'Eugenio et al. (2013), such a process could be dynamical friction. We know that SRs are far more likely to be the most massive galaxies in the cluster, and that dynamical friction is more effective for massive galaxies. One concern for this proposal is that SRs could then merge, depleting their numbers; this may *decrease* f_{SR} in dense LPEs, unless there is a mechanism to prevent this merging, such as in the *overmerging* problem (Moore et al. 1999). Perhaps FRs are transformed into SRs at the same rate that SRs merge with themselves; such delicate balance permits a uniform f_{SR} across different GHEs while also allowing for the LPE gradient that we see in individual clusters. Such a scenario is almost hierarchical and could explain why massive galaxies are more likely to be SRs; it also suggests that the most massive galaxies in any given GHE will be SRs.

This study and that of D'Eugenio et al. (2013) both find that the region of λ populated by FRs in clusters is different to the region populated by the ATLAS[3D] sample; FRs in Coma and Abell 1689 generally have $\lambda < 0.6$ whereas, the ATLAS[3D] sample populates $\lambda < 0.8$. Taken at face value, this suggests a different distribution for the intrinsic anisotropy of the galaxies: Cappellari et al. (2007) and Emsellem et al. (2011) found that the population of FRs in the $\lambda-\epsilon$ diagram could be explained by projection of anisotropic rotators, with the anisotropy distributed normally but truncated to exclude anisotropies $\delta > 0.8\epsilon_{int}$, where ϵ_{int} is the intrinsic ellipticity (i.e. not projected). The effect of truncating the anisotropy distribution is to exclude $\lambda > 0.8$. If one were to truncate at a lower anisotropy, one could similarly exclude lower values of λ. This would suggest there is a mechanism in the cluster environment that lowers the anisotropy of FRs. Studies with much larger sample sizes could better investigate changes in the distribution of FRs in the $\lambda-\epsilon$ plane. Similarly, studies of the observed ellipticity of galaxies could corroborate these claims.

Finally, we note that the dispersion maps can show strong, weak and sometimes no central dynamically hot component. These components are assumed to originate from a stellar bulge, which may be strong, weak or absent. Such *kinematic* identification of bulges may help with decomposing these galaxies into disc and bulge components, or similarly may help prevent unnecessary parametrization (and degeneracy) in the surface photometry when no kinematic bulge is evident. The lack of a hot central component in some galaxies suggests that bulges are not ubiquitous in ETGs.

5.1 Future studies

To conclusively understand the processes that create SRs, more investigation is required. Our limited sample of 27 galaxies has barely sampled the entirety of Coma. The Coma cluster is known to extend over $3°$ but we only sample galaxies within a radius of 15 arcmin (0.43 Mpc) from the cluster centre. Similarly, the study of Abell 1689 by D'Eugenio et al. (2013) was limited to the *HST*/ACS footprint (202 arcsec × 200 arcsec), which covers a (circularized) radius of only 0.35 Mpc. By comparison, a radius of 0.5 Mpc in Virgo enclosed eight of the nine SRs (Cappellari et al. 2011b); clearly future studies of the cluster outskirts are required to establish if only FRs are found outside a critical radius, which would tend to *lower* the average f_{SR} found for both Coma and Abell 1689. Furthermore, we have poor statistics on f_{SR} at lower LPE density: the presence of SRs in the low-density outskirts of clusters may challenge the need for dynamical friction. At present, although our measurements for Coma show a gradient in f_{SR} with Σ_3, the posterior uncertainties are consistent with no gradient. To improve on this result requires a much larger survey; for example, were a complete IFS survey of Coma's central square rcminute (∼150 galaxies) to find the same gradient as seen in Fig. 8, the posterior uncertainties (assuming the same binning, negligible measurement uncertainty and a binomial distribution for f_{SR}) would not overlap at the 68 per cent CI level. Such a level of accuracy would provide meaningful constraints on future model predictions. Similarly, $kT - \Sigma$ data only exists for three clusters, which is far from a representative sample, and significantly lacking compared to the 55 clusters studied by Dressler (1980). The local Universe contains many different groups and clusters (GHEs) with a range of properties which remain to be surveyed with IFS. We also have poor understanding of low-luminosity SRs, which appear to be rare. A study concentrating on intermediate GHE densities, such as groups, could help us understand if a true hierarchy exists, and if the most massive galaxies in a local volume or parent halo (GHE) always have low specific angular momentum. New multiplexed IFS instruments like SAMI (Croom et al. 2012; Fogarty et al. 2012), KMOS (Sharples et al. 2013) and MaNGA have the potential to perform these studies efficiently. A more targeted approach could study individual massive galaxies at higher redshifts in an attempt to witness the assembly of SRs, be it a sudden or gradual process.

Our theoretical understanding of the processes that create SRs is currently undergoing change. Until recently, it was widely accepted that pressure supported, slowly rotating systems were the end products of major mergers (Barnes 1988; Hernquist 1992; Naab & Burkert 2003). But the latest *N*-body simulations of binary mergers with realistic, cosmologically motivated impact parameters suggest that the orbital angular momentum becomes locked in the stars of the remnant, leading to significant specific angular momentum and flattening in all but the most elaborate (and unlikely) initial configurations (Bois et al. 2011). Given the segregation of SRs into regions of higher LPE density suggests a dominant role for dark matter, it may be revealing to run similar models inside group- or cluster-scale haloes with increased dynamical friction; we know for example that the two central SRs in Coma will eventually merge (Gerhard et al. 2007). Semi-analytic models can produce SRs if the most massive galaxies in massive haloes are allowed to cannibalize material from tidally stripped satellites (Khochfar et al. 2011). These studies now need to turn to group-like environments with lower (GHE) densities to identify if the same mechanisms can maintain a constant f_{SR} there. Furthermore, studying individual clusters in these models may explain the excess of SRs towards the densest LPEs, and the absence of SRs in the lowest density LPEs, while the average f_{SR} remains constant across different GHE densities.

6 CONCLUSION

Using the Oxford SWIFT spectrograph, we have surveyed 27 galaxies in the Coma cluster, taking care to minimize sample bias with respect to luminosity and ellipticity. We find $4 \pm^{1.7}_{1.6}$ SRs, all of which have $M_K < 24$ mag and $\epsilon < 0.4$. The average SR fraction in the Coma ETG population is thus 0.15 ± 0.06. This is identical to the average SR fraction found in the ATLAS^{3D} field/group environment as well as the Virgo and Abell 1689 clusters, suggesting no change with GHE. However, within the clusters the distribution of SRs is not uniform, but appears to be concentrated towards denser LPEs. We confirm that the SR fraction is higher at higher luminosities, and find no variation of the distribution with GHE. These results constrain the different mechanisms needed to produce the contrasting physical properties of FRs and SRs. Both mechanisms must increase in efficiency in clusters to produce the excess of ETGs observed, while at the same time maintaining a constant SR fraction inside each GHE. Conversely, the mechanism for producing FRs is more efficient at lower luminosities, but no more so across different GHEs.

We also find that the velocity dispersion maps of FRs are generally dynamically colder than the dispersion maps of SRs. Furthermore, dynamically hot central components (presumably relating to the presence of a bulge) can be seen at the centres of *some*, but not all, FRs.

REFERENCES

Bacon R. et al., 2001, MNRAS, 326, 23
Barnes J. E., 1988, ApJ, 331, 699
Binney J., 1978, MNRAS, 183, 501
Binney J., 2005, MNRAS, 363, 937
Bois M. et al., 2011, MNRAS, 416, 1654
Cappellari M., Emsellem E., 2004, PASP, 116, 138
Cappellari M. et al., 2007, MNRAS, 379, 418
Cappellari M. et al., 2011a, MNRAS, 413, 813
Cappellari M. et al., 2011b, MNRAS, 416, 1680
Cenarro A. J., Cardiel N., Gorgas J., Peletier R. F., Vazdekis A., Prada F., 2001, MNRAS, 326, 959
Croom S. M. et al., 2012, MNRAS, 421, 872
Davies R. L., Efstathiou G., Fall S. M., Illingworth G., Schechter P. L., 1983, ApJ, 266, 41
Davis M., Geller M. J., 1976, ApJ, 208, 13
D'Eugenio F., Houghton R. C. W., Davies R. L., Bontà E. D., 2013, MNRAS, 429, 1258
Djorgovski S., Davis M., 1987, ApJ, 313, 59
Dressler A., 1980, ApJ, 236, 351
Dressler A., Lynden-Bell D., Burstein D., Davies R. L., Faber S. M., Terlevich R., Wegner G., 1987, ApJ, 313, 42
Emsellem E. et al., 2011, MNRAS, 414, 888
Fogarty L. M. R. et al., 2012, ApJ, 761, 169
Fruchter A. S., Hook R. N., 2002, PASP, 114, 144
Gerhard O., Arnaboldi M., Freeman K. C., Okamura S., Kashikawa N., Yasuda N., 2007, A&A, 468, 815
Godwin J. G., Metcalfe N., Peach J. V., 1983, MNRAS, 202, 113
Graham A. W., Driver S. P., Petrosian V., Conselice C. J., Bershady M. A., Crawford S. M., Goto T., 2005, AJ, 130, 1535
Han M., Mould J. R., 1992, ApJ, 396, 453
Hernquist L., 1992, ApJ, 400, 460
Houghton R. C. W., Davies R. L., Dalla Bontà E., Masters R., 2012, MNRAS, 423, 256
Khochfar S. et al., 2011, MNRAS, 417, 845
Komatsu E. et al., 2011, ApJS, 192, 18
Krajnović D., Cappellari M., de Zeeuw P. T., Copin Y., 2006, MNRAS, 366, 787
Krajnović D. et al., 2008, MNRAS, 390, 93
Krajnović D., Emsellem E., Cappellari M., Alatalo K., Blitz L., Bois M., Bournaud F., Bureau M. E., 2011, MNRAS, 414, 2923
Moore B., Ghigna S., Governato F., Lake G., Quinn T., Stadel J., Tozzi P., 1999, ApJ, 524, L19
Muldrew S. I. et al., 2012, MNRAS, 419, 2670
Naab T., Burkert A., 2003, ApJ, 597, 893
Nowak N., Saglia R. P., Thomas J., Bender R., Pannella M., Gebhardt K., Davies R. I., 2007, MNRAS, 379, 909
Oemler A., Jr, 1974, ApJ, 194, 1
Press W. H., Teukolsky S. A., Vetterling W. T., Flannery B. P., 1992, Numerical Recipes in C. The Art of Scientific Computing, 2nd edn. Cambridge Univ. Press, Cambridge
Rusli S. P., Thomas J., Erwin P., Saglia R. P., Nowak N., Bender R., 2011, MNRAS, 410, 1223
Scott N., Houghton R., Davies R. L., Cappellari M., Thatte N., Clarke F., Tecza M., 2012, MNRAS, 425, 1521
Sharples R. et al., 2013, Messenger, 151, 21
Thatte N., Tecza M., Clarke F., Goodsall T., Lynn J., Freeman D., Davies R. L., 2006, in McLean I. S., Iye M., eds, Proc. SPIE Conf. Ser. Vol. 6269, The Oxford SWIFT Integral Field Spectrograph. SPIE, p. 62693
van Dokkum P. G., 2001, PASP, 113, 1420
Weijmans A.-M. et al., 2009, MNRAS, 398, 561
Yasuda N. et al., 2001, AJ, 122, 1104

APPENDIX A: SOURCES OF UNCERTAINTY IN λ

Here we list dominant sources of uncertainty and our approaches to quantifying and, where possible, minimizing their contribution in the calculation of λ.

A1 Random uncertainty from photon shot noise

As explained in Section 3, the formal random uncertainties in V and σ provided by PPXF originate directly from the photon noise. However, the propagation of these uncertainties through the expression for the calculation of λ from V and σ is not trivial and is not documented. We summarize the formulae for propagation here, assuming a standard first-order (Taylor expansion) approach.

A standard first-order Taylor expansion tells us that if the uncertainties are small, we can propagate random uncertainties from input parameters using the first derivatives with respect to those parameters. Thus for λ, considering only covariances between V and σ,

$$(\Delta\lambda)^2 \approx \left(\frac{\partial\lambda}{\partial F_i}\Delta F_i\right)^2 + \left(\frac{\partial\lambda}{\partial R_i}\Delta R_i\right)^2 \tag{A1}$$

$$+ \left(\frac{\partial\lambda}{\partial V_i}\Delta V_i\right)^2 + \left(\frac{\partial\lambda}{\partial \sigma_i}\Delta \sigma_i\right)^2 \tag{A2}$$

$$+ 2\frac{\partial\lambda}{\partial V_i}\frac{\partial\lambda}{\partial \sigma_i}\text{Cov}(V_i, \sigma_i). \tag{A3}$$

The first-order derivatives with respect to each input parameter are

$$\frac{\partial\lambda}{\partial F_i} = \frac{R_i|V_i|}{\sum_j F_j R_j M_j} - R_i M_i \left[\frac{\sum_k F_k R_k |V_k|}{\left(\sum_l F_l R_l M_l\right)^2}\right] \tag{A4}$$

$$\frac{\partial\lambda}{\partial R_i} = \frac{F_i|V_i|}{\sum_j F_j R_j M_j} - F_i M_i \left[\frac{\sum_k F_k R_k |V_k|}{\left(\sum_l F_l R_l M_l\right)^2}\right] \tag{A5}$$

$$\frac{\partial \lambda}{\partial V_i} = \frac{F_i R_i \mathrm{Sgn}(V_i)}{\sum_j F_j R_j M_j} - \frac{F_i R_i |V_i|}{M_i} \left[\frac{\sum_k F_k R_k |V_k|}{\left(\sum_l F_l R_l M_l \right)^2} \right] \quad (A6)$$

$$\frac{\partial \lambda}{\partial \sigma_i} = -\frac{F_i R_i \sigma_i}{M_i} \left[\frac{\sum_k F_k R_k |V_k|}{\left(\sum_l F_l R_l M_l \right)^2} \right], \quad (A7)$$

where $M_i = (V_i^2 + \sigma_i^2)^{1/2}$ and $\mathrm{Sgn}(V_i) = V_i/|V_i|$. The choices for ΔV_i and $\Delta \sigma_i$ are obvious and come straight from the standard errors provided by PPXF; ΔF_i originates from $\sqrt{N}$, where N is the number of photons collected in that bin while ΔR_i was chosen as the standard deviation of the radii of the spaxels in each bin (thus bins extending over larger radii have a larger ΔR_i). In practice, the uncertainties in V and σ dominate and the typical (mean) relative uncertainty in λ is 10 per cent.

A2 Discretization noise

It became apparent that the discretization of the velocity and velocity dispersion maps (an unavoidable consequence of binning to the S/N necessary for extraction of kinematics) leads to a source of noise in λ; different choices in the sizes and positions of the bins lead to different kinematics and measures of λ. We wish to quantify this effect in order to establish its significance. This is not trivial as most binning mechanisms are not random (and so cannot be seeded to give different configurations) but generate a single unique configuration. However, in the sector approach we use here, the azimuthal angle used to divide sectors can be rotated by a fraction of the sector width, leading to different binning choices, both azimuthally and radially. Applying different rotations, we generated many different configurations; comparing the kinematics extracted in each case allowed us to estimate the noise generated by discretization. This approach suggests that the relative uncertainty in λ from discretization of the V and σ maps is around 5 per cent which is half the typical uncertainty from photon noise and can further be reduced by use of *dithered* kinematic maps (see Section 2.5.2). It is therefore not a significant source of uncertainty.

A3 Systematic uncertainty from sky line subtraction residuals

We found that residuals from the subtraction of sky emission lines can cause a catastrophic failure in the kinematic results (the model fit not representing the underlying galaxy spectrum), leading to error in the measurement of V and σ and thus λ. Such systematics can be significantly reduced, if not removed completely, by masking strong sky lines, or simultaneously fitting the sky spectrum when fitting the kinematics in PPXF. However, masking can also remove one or more of the calcium triplet absorption lines from the fit (i.e. information on V and σ), so it is undesirable to always mask the sky emission lines; conversely, fitting the sky spectrum simultaneously retains all the absorption lines but also retains residuals from imperfect subtraction. To avoid ad hoc decisions on when to mask or simultaneously fit the sky, it is desirable to define physically motivated reasons for a systematic approach in all cases.
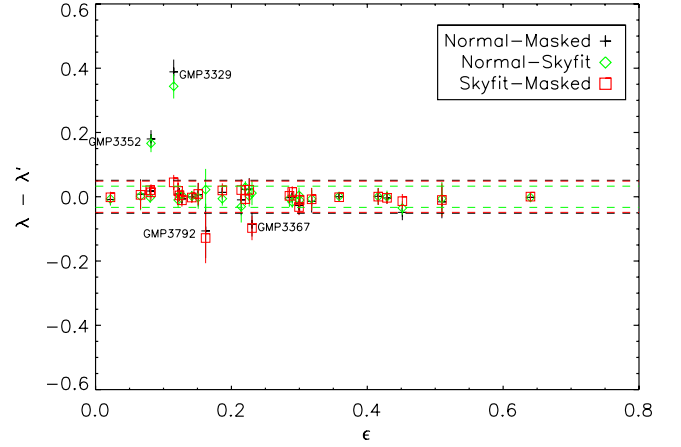

Figure A1. The difference in the calculation of λ with/without masking and simultaneous fitting of the sky spectrum. The difference in λ with and without masking is shown in black; the difference with and without simultaneous sky spectrum fitting is shown in green and the difference between masking and simultaneous fitting is shown in red. For each case, a robust estimation of the standard deviation is shown by the dashed lines.

We extracted the kinematics and measured λ (from dithered maps) with and without masking of sky emission lines and compare the results in Fig. A1 (black). Sky residuals do not bias the determination of λ in the majority of cases, but the few cases where there is an error need to be corrected. A robust estimation of the standard deviation (using the IDL ROBUST_SIGMA algorithm) gives $\sigma_{\lambda - \lambda'} = 0.017$.

As an alternative to masking the affected regions, we can fit the sky spectrum simultaneously while fitting the kinematics (as done in Weijmans et al. 2009). Fig. A1 (red) compares values of λ with and without simultaneous fitting of the sky spectrum. As before, the majority of cases show little change in λ but there are a few galaxies where λ changes significantly; a robust estimation of the standard deviation gives $\sigma_{\lambda - \lambda'} = 0.011$, which is less than the previous comparison and suggests that simultaneously fitting the sky is reducing the systematic error in λ more than masking is. For completeness, we compare λ calculated with masked spectra and with simultaneous sky fitting in Fig. A1 (green); a robust estimation of the standard deviation in this case gives $\sigma_{\lambda - \lambda'} = 0.016$, which further suggests that the masking technique is not as robust as the sky fitting technique.

There are four galaxies in Fig. A1 for which λ is very different when calculated using different techniques. Both the masking and sky fitting techniques agree on λ for GMP3329 and GMP3352; indeed, the spectral fits when using masking or sky fitting techniques are much less affected by the sky. However, the masking and sky fitting techniques disagree on λ for two galaxies: GMP3367 and GMP3792. For GMP3367, both techniques find identical velocity maps but differ slightly regarding the dispersion; however, both agree that this galaxy is an undisputed FR. For GMP3792, the masking technique shows correlated errors in V and σ for certain bins, artificially inflating λ; the sky fitting technique finds no rotation in the velocity map and provides much better fits to the spectra.

It is clear from these investigations that simultaneously fitting the sky spectrum is the most robust approach to calculating V, σ and λ; it is therefore the approach we adopt.

This paper has been typeset from a TEX/LATEX file prepared by the author.